Evaporation-driven convective flows in suspensions of nonmotile bacteria

Jocelyn Dunstan,[1,*] Kyoung J. Lee,[2] Yongyun Hwang,[3] Simon F. Park,[4] and Raymond E. Goldstein[1,†]

[1]*Department of Applied Mathematics and Theoretical Physics, Centre for Mathematical Sciences, University of Cambridge, Cambridge CB3 0WA, United Kingdom*

[2]*Department of Physics, Korea University, Seoul, Korea*

[3]*Department of Aeronautics, Imperial College, London, United Kingdom*

[4]*Faculty of Health & Medical Sciences, University of Surrey, Guildford GU2 5XH, Surrey, United Kingdom*

(Received 7 April 2017; published 28 December 2018)

We report a novel form of convection in suspensions of the bioluminescent marine bacterium *Photobacterium phosphoreum*. Suspensions of these bacteria placed in a chamber open to the air create persistent luminescent plumes most easily visible when observed in the dark. These flows are strikingly similar to the classical bioconvection pattern of aerotactic swimming bacteria, which create an unstable stratification by swimming upwards to an air-water interface, but they are a puzzle since the strain of *P. phosphoreum* used does not express flagella and therefore cannot swim. When microspheres were used instead of bacteria, similar flow patterns were observed, suggesting that the convective motion was not driven by bacteria but instead by the accumulation of salt at the air-water interface due to evaporation of the culture medium. Even at room temperature and humidity, and physiologically relevant salt concentrations, the water evaporation was found to be sufficient to drive convection patterns. To prove this hypothesis, experiments were complemented with a mathematical model that aimed to understand the mechanism of plume formation and the role of salt in triggering the instability. The simplified system of evaporating salty water was first studied using linear stability analysis, and then with finite element simulations. A comparison between these three approaches is presented. While evaporation-driven convection has not been discussed extensively in the context of biological systems, these results suggest that the phenomenon may be broadly relevant, particularly in those systems involving microorganisms of limited motility.

DOI: 10.1103/PhysRevFluids.3.123102

I. INTRODUCTION

In the deep ocean, animals such as certain fish and squid produce light through a symbiotic relationship with bioluminescent bacteria [1]. One well-known luminescent bacterium is *Photobacterium phosphoreum*, a rod-shaped organism $\sim 3.5\ \mu$m long and $\sim 0.5\ \mu$m wide, whose bright luminescence can easily be observed when a flask containing a sufficiently concentrated suspension

*Present address: Institute of Biomedical Sciences (ICBM), Faculty of Medicine / Center for Mathematical Modeling (CMM), Faculty of Physical and Mathematical Sciences, Universidad de Chile, Santiago, Chile.

†Corresponding author: R.E.Goldstein@damtp.cam.ac.uk

Published by the American Physical Society under the terms of the Creative Commons Attribution 4.0 International license. Further distribution of this work must maintain attribution to the author(s) and the published article's title, journal citation, and DOI.

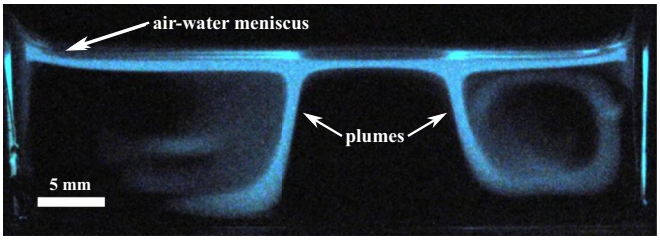

FIG. 1. Convective flow observed in a suspension of *Photobacterium phosphoreum*. The chamber is 6 cm long, 1 mm deep, and 1 cm high. Bacteria were cultured to a density of 5.5×10^8 cells/cm^3 following the procedure detailed in the text. This image was acquired with a Nikon D300s equipped with a 60 mm f/2.8 macro lens, and an exposure time of 10 seconds.

is swirled gently to oxygenate the fluid. If, instead, the suspension is placed in a cuvette like that shown in Fig. 1, then after a period of several minutes, within which the bacteria deplete the oxygen and bulk luminescence fades away, a novel phenomenon of bright convective plumes is observed. In the figure, which was taken with no external illumination, blue regions are luminescent and have a high concentration of oxygen. Careful observation shows that the fluid within the plumes flows downward from the meniscus and the luminescence within gradually fades as the fluid descends and recirculates in convective rolls. The chemical reaction by which *P. phosphoreum* produces light is catalyzed by the enzyme luciferase, where flavin mononucleotide ($FMNH_2$) and a long-chain aldehyde (RCHO) are combined with molecular oxygen (O_2) to produce photons at 490 nm [2]. The emission of light only occurs when the cell concentration is high enough, which is known as *quorum sensing* [2], but also when the oxygen concentration is above 0.015 μM, and then is approximately constant for higher oxygen concentrations, similar to a step function [3]. This last point explains why in the images the interface between dark and bright regions is sharp: only above a threshold of oxygen concentration is there light emission, which corresponds to the interface observed in the experiments.

The convection pattern in Fig. 1 appears to be a classic example of bioconvection [4], an instability that arises from the accumulation of swimming microorganisms at the top surface of a suspension, typically in response to chemical gradients or light. As most cells are denser than the suspending fluid, upwards chemo- or phototaxis creates an unstable nonuniformity in the cell concentration which triggers convective motion. Yet, the strain of *P. phosphoreum* used in our experiments is nonmotile under the given conditions, presumably as a consequence of generations of culturing in rich media in which expression of flagella is not triggered. Given this, the macroscopic flow in Fig. 1 cannot be rationalized as a classical bioconvective instability.

An alternate explanation for the observed convective patterns is that a metabolic reaction—for example, the chemical reaction that produces bioluminescence—releases a component that is denser than the background fluid. Precedent for this comes from the phenomenon of *chemoconvection*, as in the methylene-blue glucose system, where a reaction product alters the local buoyancy balance [5]. Using similar arguments, Benoit *et al.* [6] explained the buoyant plumes observed in a suspension of nonmotile *Escherichia coli* consuming glucose. As will be explained in detail below, a series of control experiments allows us to discard the hypothesis that a chemical reaction or metabolic activity creates the plumes. Instead, we find that the convection arises from evaporation of the salty suspension.

During evaporation, cooling of the air-liquid interface changes the nearby fluid density. Unless a stabilizing negative gradient of temperature is imposed, the thermal component will also be present when studying evaporation-driven convection. An early study of the change in density in an evaporating fluid was presented by Spangenberg and Rowland [7], who analyzed the fluid composition with Schlieren photography, exploiting the change of the refractive index as a function of density. They obtained plunging regions when the fluid was allowed to evaporate at room

temperature. A similar experiment was reported by Berg *et al.* [8], who investigated pure and mixed fluids as well as the effect of impurities at the surface. Traditionally, the Sherwood number (defined as the ratio between convective mass transfer and diffusion rate) has been used to characterize evaporating surfaces [9]. More recent studies have looked closely at evaporating layers [10], binary liquid layers [11], and liquid films [12].

As presented here, the thermal component was verified not to be dominant in the plume formation in *P. phosphoreum*. Instead, we find that the salt concentration in the suspension determines the time required to observe the instability, its wavelength, and the flow speed. Another effect that may have a role when a fluid evaporates is the change in surface tension. Such Marangoni flows occur because a fluid with higher surface tension pulls laterally more strongly, and therefore a gradient in surface tension will generate accumulation of fluid in certain regions [13]. If the liquid contains particles, they will accumulate in regions of high surface tension. But the converse is also true: a higher concentration of particles increases surface tension [14]. We find examples of Bénard-Marangoni instability in the context of drying liquid films [15], liquid layers [16], polymer solutions [17], and volatile binary fluids [18]. Since temperature also changes the surface tension, there is a complex interplay of effects in a drying fluid [19]. In the model presented here we find that it is not necessary to include changes in the surface tension to explain the instability, and therefore we conclude that surface tension is also not the driving force in the experiments presented here.

A prior report of evaporation-induced convection in a salty water was presented by Kang *et al.* [20], where flows in a sessile droplet were observed by adding fluorescent microspheres. They noticed that the flow was first oriented towards the perimeter of the drop, in the same way as it moves in the coffee stain phenomenon [21,22]. An accumulation of salt occurs at the surface of the drop, which triggers convective motion. The proposed mathematical model introduces the "salinity Rayleigh number" Ra_s by analogy with the Rayleigh number used to predict the onset convection in a fluid heated from below [23]. The salinity Rayleigh number compares the buoyancy generated by the accumulation of salt with the stabilizing effects of salt diffusion and fluid viscosity. This concept has been used previously in the literature to explain the double-diffusion in the phenomenon of salt fingering [24], and it has been also found to be essential to understand the accumulation of salt in saline groundwater lakes [25].

This paper is organized as follows: Sec. II describes the experimental setup and quantitative observations of plumes, first using bacteria and culture medium, and then a simplified version of microspheres in salty water. In the next two sections a mathematical model is introduced in order to understand the plumes observed in experiments. This model is based on the coupling of the Navier-Stokes equation for the evaporating fluid with an advection-diffusion equation for the salt. The model is first studied in Sec. III using linear stability analysis, and then numerically using a finite element method in Sec. IV. A comparison between experiments, linear stability analysis, and numerical results is presented in Sec. V. Finally, conclusions and future work are summarized in Sec. VI.

II. EXPERIMENTAL METHODS AND RESULTS

A. Culturing of *P. phosphoreum*

Table I lists the ingredients for the liquid and solid media used in the experiments with *P. phosphoreum*. These are mixed with distilled water up to 1 liter and then autoclaved for sterility. Bacterial cultures were streaked on agar plates and kept in an incubator at 19 °C in the dark, and renewed every two weeks. Liquid cultures were prepared by picking a bright colony from an agar plate and adding it to 50 ml of bacterial culture, which was then shaken at 100 rpm in an incubator in the dark at 19 °C. For long-term storage, the strain was frozen at −80 °C using the cryoprotective medium described by Dunlap and Kita-Tsukamoto [2], although using 65% (by volume) glycerol in equal parts worked equally well. Bacterial concentrations were estimated from $\mathrm{OD}_{600\,\mathrm{nm}}$, the optical density at 600 nm, a measure of the turbidity of a suspension, quantified

TABLE I. Liquid and solid media used to grow *P. phosphoreum*.

Liquid medium (for 1 liter)		Solid medium (for 1 liter)	
peptone	10 g	nutrient broth powder	8 g
sodium chloride	30 g	sodium chloride	30 g
glycerol	2 g	glycerol	10 g
dipotassium hydrogen phosphate	2 g	calcium carbonate	5 g
magnesium sulphate	0.25 g	agar	15 g

using a spectrophotometer emitting light at that frequency [26]. A calibration between OD and bacterial concentration was constructed for *P. phosphoreum* using serial dilution and the track method. It showed that $OD_{600\,nm} = 1$ corresponds to 5×10^8 bacteria/ml, the density used in all the experiments.

B. Observational setup

Suspensions were studied in chambers of the shape shown in Fig. 2(a), constructed using two glass coverslips (Fisher 12404070), held together by two layers of tape 300 μm thick (Bio-Rad SLF-3001). This tape has internal dimensions 6×2 cm, and one long side was cut to create an air-liquid interface. The cuvette, 600 μm in depth, was filled using a plastic syringe connected to a stainless steel needle (Sigma-Aldrich CAD4108) to yield a fluid height of 1 cm, which was the initial condition for all the experiments and for the model presented in Secs. III and IV.

Figure 2(b) is a schematic illustration of the darkfield imaging setup used to observe the plumes: from left to right, a charge-coupled device (CCD) camera (Hamamatsu C7300), the sample (blue), and a darkfield LED ring (Stemmer Imaging, CCS FPR-136-RD). The camera is placed outside the light cones formed by the red LED-ring illuminator. The particles (bacteria or microspheres) suspended in the sample are visible by the light they scatter into the camera.

This setup can also be used to capture bacterial bioluminescence and darkfield images *quasi-simultaneously* by switching on and off the LED ring in synchrony with acquisition of images. This was achieved by adding a second camera at the other side of the ring and synchronizing both cameras and the LED ring using an Arduino board (UNO-R2). The result is shown in Fig. 3 where one can see a plume magnified (darkfield image at left, image of bioluminescence at right). We observe two key points. First, the darkfield imaging system permits the observation of plumes beyond the region where oxygen is high enough to produce bioluminescence. In other words, when looking at bioluminescent images with camera #2 we only see regions with enough oxygen to create

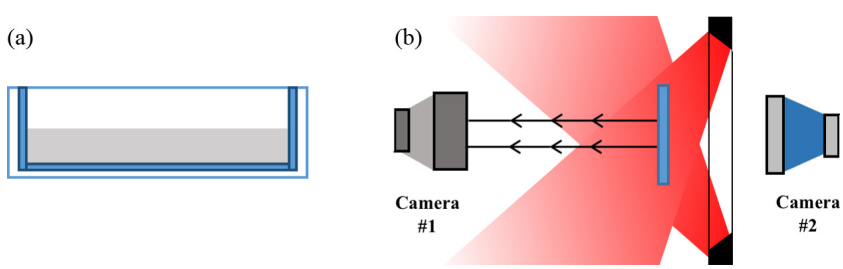

FIG. 2. Experimental setup. (a) Cuvette used in the experiment made with two coverslips held together by 600 μm thick tape cut in a U shape. (b) dual (darkfield and luminescence) imaging system. For the darkfield imaging, an LED-ring is used for sample illumination while camera #1 (left) is placed in the darkfield so that image will be formed only when scattered light from the sample reaches the camera. During the bioluminescence imaging with camera #2 (right), the darkfield LED ring was turned off.

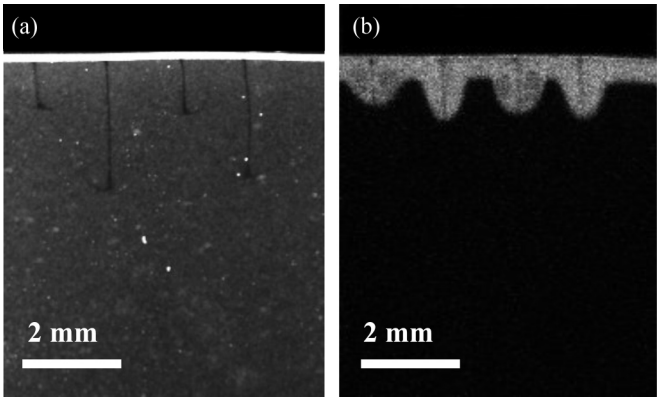

FIG. 3. Magnified image of a plume in a suspension of *P. phosphoreum*, compared between darkfield (left) and bioluminescence image (right). The optical density was $OD_{600\,nm} = 1$ and the scale bar is 2 mm.

bioluminescence, while the darkfield setup allows the detection of changes in particle or bacterium density, which extends deeper in the fluid than the oxygen carried from the top surface. Second, the center of each plume is *depleted of bacteria*, and they appear as dark regions in both images. This somewhat puzzling observation becomes understood once the mechanism of plume formation is clarified in the next sections.

C. Control experiments

The hypothesis that the chemical reaction leading to light production in *P. phosphoreum* creates dense components that trigger hydrodynamic plumes was excluded after two control experiments. The first one consisted of placing nonmotile, nonbioluminescent bacteria in the same experimental setup. A genetically modified strain of *Serratia* (ATCC 39006), provided by Dr. Rita Monson (Department of Genetics, University of Cambridge), also created the plumes observed with *P. phosphoreum*, even though this bacterium does not produce light when it consumes oxygen. The second and most important control experiment came from using 3 μm diameter polystyrene beads (Polyscience 18327, density 1.05 g/cm^3) at a similar optical density (OD) as in the experiments with *P. phosphoreum*. Figure 4 shows side-by-side experiments with (a) bacteria and (b) beads suspended in the same bacterial medium (detailed in Table I) and observed using the darkfield LED-ring technique. In these experiments the upper boundary of the cuvette was sealed except for one small hole (indicated by an arrow) which allowed evaporation. We found that in both cases

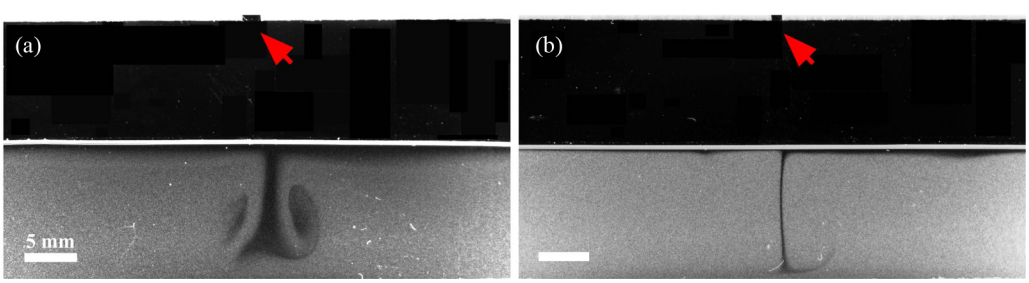

FIG. 4. Control experiments. *P. phosphoreum* (a) and 3 μm beads (b) were placed in cuvettes (Fig. 2), but with a upper boundary sealed except for a single hole (red arrows). Both experiments were performed at optical density $OD_{600\,nm} = 1.5$, using the same liquid medium, and the images were taken 75 minutes after the experiment started.

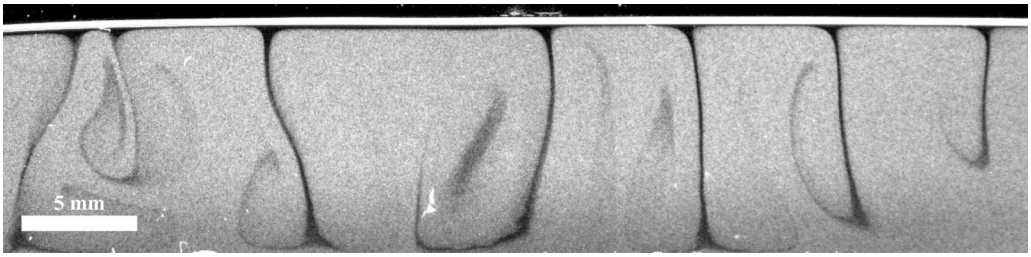

FIG. 5. Convection in a microsphere suspension. Darkfield image of the plumes observed in a suspension of 3 μm diameter beads with 1% (w/w) salt concentration. The optical density was $OD_{600\,nm} = 1$ and the image was taken 30 minutes after the experiment had started.

the position of the plume is correlated with the position of the source of evaporation, which can be understood with the model of plume formation proposed later. As also observed in Fig. 3, the center of the plumes is depleted of bacteria or beads in both cases. Videos of these two experiments are provided in the Supplemental Material [27].

As plume generation evidently does not depend on any life processes of the bacteria, in subsequent experiments described below we focused exclusively on suspensions of microspheres instead of bacteria. Switching to beads also allowed us to explore a wide range of salt concentrations, far beyond that which is physiologically possible using *P. phosphoreum*, and therefore bacterial medium was substituted by aqueous solutions of salt at various concentrations.

D. Experiments using microspheres

Figure 5 shows convective patterns observed in a suspension of 3 μm diameter microspheres at $OD_{600\,nm} = 1$ with a salt concentration of 1% (by weight, or w/w). The bright horizontal line at the top of the image is the air-water meniscus. As previously noted, the plumes appear dark in the darkfield image, which implies the absence of beads scattering light in those regions. This situation is very different from conventional bioconvection, in which plumes appear bright due to the relatively higher bacterial concentration within them. The video from which Fig. 5 was extracted is Video 3 of the Supplemental Material [27].

A protocol was designed to find the positions of the plumes as they vary over time. An image, such as Fig. 5, was cropped vertically near the upper surface, converted to black and white with a threshold of 0.5, and inverted to create bright plumes. A one-dimensional plot was generated by averaging the pixel intensity vertically, where noise was reduced by applying the MATLAB function *smooth*. Peaks were found using the function *findpeaks*, with the empirical requirement of a minimum spacing between peaks of 0.4 mm. Figure 6 shows the plume positions corresponding to the experiment in Fig. 5, where different colors represent the position of the first plume, second plume, and so on until the seventh. In this representation, a given plume changes color when a new plume appears at the left side.

Figures 7(a) and 7(b) show convection in suspensions with 0.1% and 0.01% (w/w) salt. Comparing these images to that in Fig. 6 one can see that for smaller salt concentrations the thickness of the plumes and the spacing between them both increase. We found the wavelengths to be $\lambda_{exp,1\%} = 0.67 \pm 0.06$ cm and $\lambda_{exp,0.1\%} = 1.58 \pm 0.08$ cm, while in 0.01% suspensions the wavelength approached the lateral dimensions of the chamber. We find that the time it takes for the appearance of plumes greatly increases as the salt concentration decreases. This can be seen in Fig. 7 where both images were taken once the instability developed: after 1 hour for 0.1% salt, but after a full 10 hours at 0.01%.

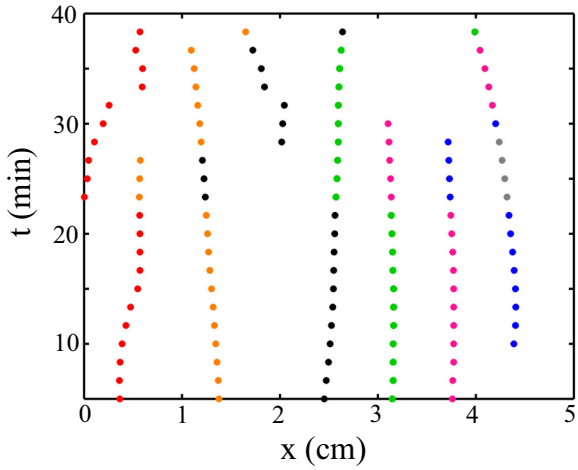

FIG. 6. Plume dynamics. Graphical representation of the plume position in time for an experiment using 3 μm diameter beads and 1% (w/w) salt concentration. Different colors indicate the position of the first plume (red), second (orange), third (black), fourth (green), fifth (pink), sixth (blue), and seventh (grey).

E. Plume mechanism

Thickness of plumes. In the experiments, the plumes appear black in the darkfield LED-ring images, which means that there are no beads (or bacteria) inside the plumes. Our hypothesis is that these dark plumes are a consequence of the sedimentation of beads: while salt is accumulating at the upper surface due to water evaporation, the beads continuously sediment, and once the instability starts (driven by salt accumulation), the convective flow carries down fluid from the top surface, which is depleted of beads, resulting in dark plumes. We would expect the thickness of the depleted layer to scale with the settling speed $v_s = 2\Delta\rho g R^2/9\eta$ of the spheres, and hence quadratically in R.

This idea was tested by performing experiments using beads of different sizes. Figure 8 shows a plume observed using monodispersed polystyrene beads of (a) 3 μm in diameter (Polyscience 09850-5) and (b) 6 μm in diameter (Polyscience 07312-5), both made with the same material of density 1.05 g/cm^3. The salt concentration in both cases was kept constant and equal to 1% (w/w) and the concentration of beads in both cases is $\mathrm{OD}_{600\,\mathrm{nm}} = 1$. Using the software IMAGEJ the plume thickness was measured at three different points, obtaining $d_{3\,\mu\mathrm{m}} = 0.152 \pm 0.008$ mm and $d_{6\,\mu\mathrm{m}} = 0.590 \pm 0.025$ mm. The ratio between these two is ~ 3.88, very close to the ratio 4 predicted by the Stokes formula above, consistent with the idea that the plume width is set by the volume of the depleted fluid layer. The volume fraction of beads is $\sim 10^{-4}$, sufficiently low that we expect no significant corrections to the settling speed nor significant buoyancy effects. It is important to note that while the nature of the experimental setup we used required microspheres for visualization, their

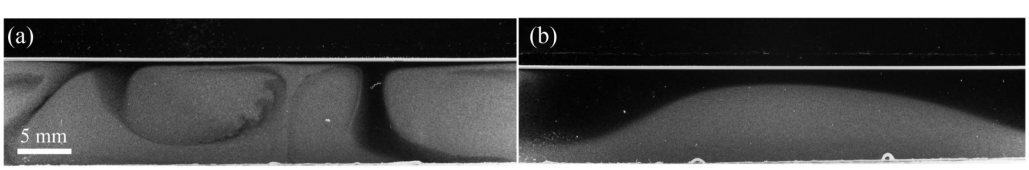

FIG. 7. Plumes at different salt concentration using 2.17 μm polyestyrene beads. (a) 0.1% (w/w) salt concentration, 1 hour after beginning of the experiment. (b) 0.01% (w/w) salt concentration, 10 hours after the experiment started. The initial height for both experiments was 1 cm, and in the image on the right the effect of evaporation can be seen by the lower meniscus.

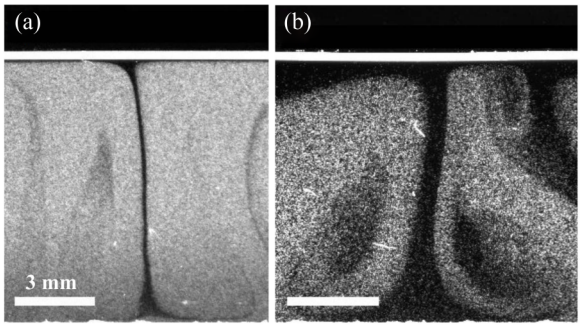

FIG. 8. Effect of microsphere size. (a) Plumes using 3 μm diameter beads and (b) 6 μm beads. The material, initial height, and salt concentration are the same in both cases. The optical density in both experiments is $\mathrm{OD}_{600\,\mathrm{nm}} = 1$ and the images were taken 45 minutes after the experiment had started.

concentration is sufficiently low that hydrodynamic interactions between them can be neglected, and are explicitly absent in the mathematical model developed below.

The dependence on salt concentration. The importance of salt in the plume formation was tested by suspending beads in pure water. In an experiment repeated in triplicate, no plumes appeared after 27 hours of observation, confirming that the presence of salt is necessary to create the convection. Room temperature and humidity conditions were checked in a 24-hour period, finding that the temperature was $21.5 \pm 0.5\,^{\circ}$C and humidity was $38 \pm 2\%$. These experiments also confirmed that the thermal effect of evaporation, that cools the upper surface and therefore makes the fluid in that region slightly heavier, is not strong enough to produce plumes under our experimental conditions. In the model presented in the next sections, thermal effects were not considered, and similar plumes were observed, suggesting that salt in the main driver in the instability presented here.

The need for evaporation. Finally, experiments of beads suspended in salty water were repeated with a layer of mineral oil at the top surface, which strongly prevents evaporation. For the same conditions as in the experiments shown in Fig. 5 [1% (w/w) salt concentration and bead concentration of $\mathrm{OD}_{600\,\mathrm{nm}} = 1$], no plumes were observed after 10 hours. The importance of evaporation was also noticed in experiments such as the one in Fig. 4, in which plumes appeared only in regions where evaporation occurs.

Hypothesis. Our experimental results have shown that (a) the center of the plumes is depleted of beads, (b) the thickness of the plumes is directly related to the sedimentation rate of beads, (c) plumes do not appear when beads are suspended in pure water, and (d) evaporation is needed to observe plumes. Based on these observations, the following hypothesis for plume formation is proposed for a system which is initially homogeneous in both bead and salt concentrations. Before the instability starts, beads sediment while evaporation occurs, leading to an accumulation of salt near the air-water interface. When the salt concentration at the top surface reaches a critical value, the hydrodynamic instability is triggered by a buoyancy imbalance, carrying down the fluid near the top surface which contains no beads.

III. LINEAR STABILITY ANALYSIS

The hypothesis that accumulation of salt due to evaporation is responsible for plume formation is studied in this section using linear stability analysis. A classical example of the use of this technique is in explaining Rayleigh-Bénard convection, observed when a fluid is heated from below, in which an instability arises as a consequence of the thermal expansion of the fluid. Bénard's observations in 1900 [28] were followed by Rayleigh's analytical work in 1916 [23], which established that the instability takes place when what we now term the Rayleigh number Ra exceeds a critical value. $\mathrm{Ra} = \beta_T \alpha g d^4/\kappa\nu$ compares the buoyancy force with the dissipative forces (viscosity and

thermal diffusion), where β_T is the temperature gradient, α the coefficient of thermal expansion, g the acceleration due to gravity, d the depth of the fluid layer, κ the thermal diffusivity, and ν the kinematic viscosity.

The calculation presented here uses a salinity Rayleigh number based on the initial fluid depth h_0,

$$\mathrm{Ra}_s = \frac{\beta c_T g h_0^3}{D\nu}, \tag{1}$$

that compares salt-induced buoyancy with the stabilizing effects of diffusion and viscosity, where β is the solute expansion coefficient (giving the change in suspension density due to salt), c_T is the initial salt concentration distributed homogeneously in space, and D is the salt diffusion constant. It is important to note that Ra_s has often been defined in the literature using the *change* in salinity between top and bottom instead of the initial salt concentration (see for example Ref. [29]). Yet, even an initially uniform concentration profile will create a gradient due to evaporation, so the present definition is more useful here, and was adopted by Kang *et al.* [20].

A. Governing equations

The problem analyzed here is a laterally infinite two-dimensional cuvette filled with a saline solution. The initial depth of the solution is h_0. The upper boundary is a free surface located at $z^* = h(t^*) + \eta(x,t)$ with $\int \eta\, dx = 0$, where h is the mean surface height and η is the location of the interface relative to h. The lower boundary is a solid wall located at $z^* = 0$. Along the free surface, we also assume that any effect of surface tension (e.g., Marangoni effect) is negligible. Evaporation has the effect of decreasing the fluid height $h(t^*)$ at a constant speed v_e, so

$$h(t^*) = h_0 - v_e t^*. \tag{2}$$

The salt concentration c^* is initially homogeneous with a value c_T and the initial height of the water column is h_0 (1 cm in the experiments). For the fluid flow, the Navier-Stokes equations within the Bousinesq approximation are used:

$$\nabla \cdot \mathbf{u}^* = 0, \tag{3a}$$

$$\frac{\partial \mathbf{u}^*}{\partial t^*} + \mathbf{u}^* \cdot \nabla \mathbf{u}^* = -\frac{\nabla p^*}{\rho_0} + \nu \nabla^2 \mathbf{u}^* - \frac{\beta(c^* - c_T)}{\rho_0} g \hat{\mathbf{k}}, \tag{3b}$$

where $\Delta\rho \equiv \beta(c^* - c_T)$ is the density difference from the uniform salt distribution (see also [20]). The boundary conditions are

$$\frac{D\eta}{Dt^*} = 0 \quad \text{at } z^* = h(t^*) + \eta, \tag{3c}$$

$$\mathbf{u}^* = 0 \quad \text{at } z^* = 0. \tag{3d}$$

Equation (3a) is the incompressibility condition, and, in Eq. (3b), p^* is the pressure difference from the hydrostatic one, with ρ_0 the fluid density in the initial state with a homogenous distribution of salt, ν the kinematic viscosity, g the acceleration of gravity, and $\hat{\mathbf{k}}$ the unit vector in the vertical direction. The dynamics of the salt concentration c^* follow the advection-diffusion equation

$$\frac{\partial c^*}{\partial t^*} + \nabla \cdot (c^* \mathbf{u}^*) = D \nabla^2 c^*, \tag{4a}$$

with D the salt diffusion constant and $\mathbf{u}^*$ the velocity field. The boundary conditions are

$$(-\mathbf{u} c^* + D \nabla c^*) \cdot \hat{\mathbf{k}} = \left(v_e - \frac{\partial \eta}{\partial t^*} \right) c^* \quad \text{at } z^* = h(t^*) + \eta^*, \tag{4b}$$

$$\nabla c^* \cdot \hat{\mathbf{k}} = 0 \quad \text{at } z^* = 0. \tag{4c}$$

Here, we note that the upper boundary condition is obtained by considering conservation of total salt concentration on decreasing $h^*(t^*)$ in time (see the Appendix for further details), although it can also be understood as compensating the amount of the lost salt concentration due to the decreasing $h(t^*)$ through an incoming advection-diffusion flux. At the lower boundary, a no-flux condition holds.

To account for the moving top boundary we normalize the vertical direction by the instantaneous height $h(t^*)$, while the horizontal direction is normalized by h_0. Furthermore, since the plume is an outcome of the gravitational overturning, the dimensionless time scale is chosen by considering the balance between gravitational and diffusion forces. This results in the dimensionless space and time scales

$$z = \frac{z^*}{h(t^*)}, \quad x = \frac{x^*}{h_0}, \quad t = \frac{\beta c_T g h_0}{D} t^*. \tag{5}$$

With these definitions, we obtain a dimensionless height and the Péclet number

$$H = \frac{h(t)}{h_0}, \quad \mathrm{Pe} = \frac{h_0 v_e}{D}, \tag{6}$$

respectively. Velocity, pressure, and salt concentration are also made dimensionless, as

$$\mathbf{u} = \frac{h_0}{D}\mathbf{u}^*, \quad p = \frac{1}{\rho_0 \beta c_T g h_0} p^*, \quad c = \frac{c^*}{c_T}. \tag{7}$$

In the resulting dimensionless equations of motion we adopt the notation $\mathbf{u} = (u, w)$ to identify the horizontal and vertical components of the fluid velocity. The incompressibility condition is

$$\frac{\partial u}{\partial x} + \frac{1}{H}\frac{\partial w}{\partial z} = 0, \tag{8}$$

and the Navier-Stokes equations are

$$\frac{\partial u}{\partial t} = -\frac{1}{\mathrm{Ra}_s \mathrm{Sc}}\left[\mathrm{Pe}\frac{z}{H}\frac{\partial u}{\partial z} - u\frac{\partial u}{\partial x} - \frac{w}{H}\frac{\partial u}{\partial z}\right] - \frac{\partial p}{\partial x} + \frac{1}{\mathrm{Ra}_s}\left(\frac{\partial^2 u}{\partial x^2} + \frac{1}{H^2}\frac{\partial^2 u}{\partial z^2}\right), \tag{9}$$

in the horizontal direction, and

$$\frac{\partial w}{\partial t} = \frac{1}{\mathrm{Ra}_s \mathrm{Sc}}\left[-\mathrm{Pe}\frac{z}{H}\frac{\partial w}{\partial z} - u\frac{\partial w}{\partial x} - \frac{w}{H}\frac{\partial w}{\partial z}\right] - \frac{1}{H}\frac{\partial p}{\partial z} + \frac{1}{\mathrm{Ra}_s}\left(\frac{\partial^2 w}{\partial x^2} + \frac{1}{H^2}\frac{\partial^2 w}{\partial z^2}\right) - (c-1), \tag{10}$$

in the vertical direction, where $\mathrm{Sc} = \nu/D$ is the Schmidt number and Ra_s is the salinity Rayleigh number in Eq. (1). The dynamics of the salt concentration is then

$$\frac{\partial c}{\partial t} = -\frac{1}{\mathrm{Ra}_s \mathrm{Sc}}\left[\mathrm{Pe}\frac{z}{H}\frac{\partial c}{\partial z} + \frac{\partial^2 c}{\partial x^2} + \frac{1}{H^2}\frac{\partial^2 c}{\partial z^2} - u\frac{\partial c}{\partial x} - \frac{w}{H}\frac{\partial c}{\partial z}\right]. \tag{11}$$

Finally, the dimensionless height evolves as

$$H(t) = 1 - \frac{\mathrm{Pe}}{\mathrm{Ra}_s \mathrm{Sc}}\, t. \tag{12}$$

The typical values of the experimental and material parameters are given in Table II. Here, it is important to note that the typical values of Ra_s for the onset of the gravitational instability have been found to be $O(10^4)$ (see also Figs. 10 and 11). Given the large Sc ($=10^3$) and the small Pe ($=0.2$), this clearly indicates that the temporal evolution of the height is much slower than that of the plumes. This enables us to rewrite the dimensionless height as $H(T) = 1 - T$ in terms of a slowly varying time $T = \delta t$, where $\delta(\equiv \mathrm{Pe}/\mathrm{Ra}_s\mathrm{Sc}) \sim O(10^{-8})$.

TABLE II. Numerical values of the parameters used in the calculations.

Parameter	Symbol	Value
Kinematic viscosity of water	ν	10^{-6} m^2/s
Salt diffusion constant	D	10^{-9} m^2/s
Salt expansion coefficient	$\beta = \rho_0^{-1}\partial\rho/\partial c$	0.007 (w/w)$^{-1}$
Initial height	h_0	10^{-2} m
Evaporation rate	v_e	2×10^{-8} m/s
Péclet number	$\mathrm{Pe} = h_0 v_e/D$	0.2
Schmidt number	$\mathrm{Sc} = \nu/D$	10^3

B. Base state

The base state is assumed to be homogeneous in the x direction, so continuity enforces $\partial w/\partial z = 0$. Given the boundary condition $w = 0$ at $z = 0$ and $\partial w/\partial z = 0$ at $z = 1$, the fluid must be at rest, i.e., $\mathbf{u}_0(t, z) = (0, 0)$. Similarly, $c = c_0(z, t)$ satisfies Eq. (11) in the absence of fluid flow. Since the dimensionless height H has been shown to be a function of the slowly varying time T [see (12)], the equation for the salt concentration in the base state is

$$\frac{\partial c_0}{\partial T} = \frac{1}{\mathrm{Pe}H^2}\frac{\partial^2 c_0}{\partial z^2} - \frac{z}{H}\frac{\partial c_0}{\partial z}, \tag{13a}$$

with the boundary conditions

$$\frac{\partial c_0}{\partial z} = \mathrm{Pe}Hc_0 \quad \text{at } z = 1, \tag{13b}$$

$$\frac{\partial c_0}{\partial z} = 0 \quad \text{at } z = 0. \tag{13c}$$

All the terms in Eq. (13) and their time dependence are of order unity, suggesting that the base state indeed evolves on a time scale of $O(T)$. Equation (13) with an initial condition $c_0(z, t = 0) = 1$ was solved numerically, with results shown in Fig. 9, where different colors represent the salt profiles after a given numbers of hours. In the figure it is clear how salt accumulates near $z = 1$, and how the overall concentration increases as a result of the decrease in height while the total amount of salt is conserved.

C. Linearized equations for small perturbations

The equations for the base state (13) reveal clearly that the time scale of evaporation is much longer than the turnover time scale of plumes observed; indeed, the time scale required to evaporate the suspension completely, around 50–100 hours, is much longer than the tens of minutes over which plumes develop. The linear stability analysis can benefit from this feature. The standard multiple time-scale analysis allows us to linearize Eqs. (9)–(11) by considering the following form of small perturbations around the base state:

$$\mathbf{u}(\mathbf{x}, t) = \mathbf{0} + \varepsilon[\mathbf{u}'(\mathbf{x}, t, T) + \delta\mathbf{u}_1'(\mathbf{x}, t, T) + O(\delta^2)] + O(\varepsilon^2), \tag{14a}$$

$$c(\mathbf{x}, t) = c_0(z, T) + \varepsilon[c'(\mathbf{x}, t, T) + \delta c_1'(\mathbf{x}, t, T) + O(\delta^2)] + O(\varepsilon^2), \tag{14b}$$

$$p(\mathbf{x}, t) = p_0(z, T) + \varepsilon[p'(\mathbf{x}, t, T) + \delta p_1'(\mathbf{x}, t, T) + O(\delta^2)] + O(\varepsilon^2), \tag{14c}$$

where $\varepsilon \ll 1$, $\mathbf{u}' = (u', w')$ is the perturbed velocity field, and c' is the perturbed salt concentration at the leading order, and $\mathbf{u}_1'$ and c_1' are their corrections due to the presence of the multiple time scale

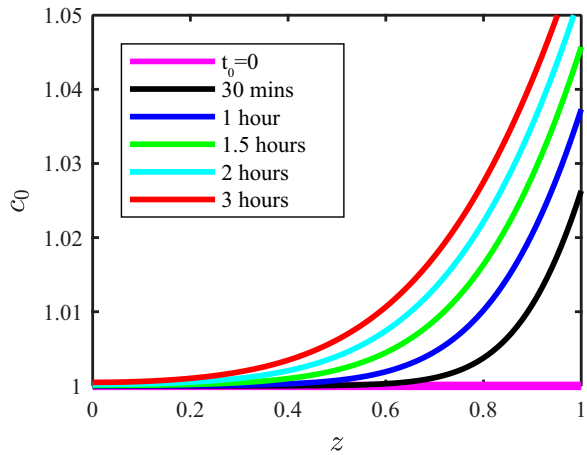

FIG. 9. Base state. Normalized salt concentration as a function of the normalized z direction. The plot corresponds to the numerical solution of Eq. (13) with no-flux boundary conditions (13b) and no flux at $z = 0$, with Pe $= 0.2$, calculated from experimental parameters. The colors correspond to different elapsed times since start of evaporation.

at $O(\delta)$. Substituting Eqs. (14) into Eqs. (9)–(11), and collecting the terms at $O(\varepsilon)$, we obtain

$$0 = \frac{\partial u'}{\partial x} + \frac{1}{H(T)}\frac{\partial w'}{\partial z}, \tag{15a}$$

$$\frac{\partial u'}{\partial t} = -\frac{\mathrm{Pe}}{\mathrm{ScRa}_s}\frac{z}{H(T)}\frac{\partial u'}{\partial z} - \frac{\partial p'}{\partial x} + \frac{1}{\mathrm{Ra}_s}\left(\frac{\partial^2 u'}{\partial x^2} + \frac{1}{H^2(T)}\frac{\partial^2 u'}{\partial z^2}\right), \tag{15b}$$

$$\frac{\partial w'}{\partial t} = -\frac{\mathrm{Pe}}{\mathrm{ScRa}_s}\frac{z}{H(T)}\frac{\partial w'}{\partial z} - \frac{1}{H(T)}\frac{\partial p'}{\partial z} + \frac{1}{\mathrm{Ra}_s}\left(\frac{\partial^2 w'}{\partial x^2} + \frac{1}{H^2(T)}\frac{\partial^2 w'}{\partial z^2}\right) - c', \tag{15c}$$

$$\frac{\partial c'}{\partial t} = \frac{1}{\mathrm{ScRa}_s}\left(-\mathrm{Pe}\frac{z}{H(T)}\frac{\partial c'}{\partial z} + \frac{\partial^2 c'}{\partial x^2} + \frac{1}{H(T)^2}\frac{\partial^2 c'}{\partial z^2} - \frac{w'}{H(T)}\frac{\partial c_0}{\partial z}\right). \tag{15d}$$

Here, it should be noted that the unsteady effect of the base state and the coefficient $H(T)$ appears only from the equations at $O(\epsilon\delta)$ because the evaporation speed is so small (i.e., $\delta \ll 1$). Therefore, at the leading order, the base state and H at a given $t = T$ can be considered to be locally "frozen" over the time scale of instability.

Equations (15d) and (15c) can be reduced to two coupled equations by introducing the stream function $\psi(x, z, t)$, which satisfies

$$u' = \frac{1}{H}\frac{\partial \psi}{\partial z} \quad \text{and} \quad w' = -\frac{\partial \psi}{\partial x}. \tag{16}$$

Taking $(1/H)\partial/\partial z$ of Eq. (15b) and subtracting $\partial/\partial x$ of Eq. (15c), we obtain

$$\frac{\partial}{\partial t}\hat{\triangle}\psi = \frac{\mathrm{Pe}}{\mathrm{ScRa}_s}\frac{z}{H}\frac{\partial}{\partial z}\hat{\triangle}\psi + \frac{1}{\mathrm{Ra}_s}\hat{\triangle}^2\psi + \frac{\partial c'}{\partial x}, \tag{17}$$

where $\hat{\triangle} = \partial^2/\partial x^2 + (1/H^2)\partial^2/\partial z^2$. Then, the equation for the perturbed salt concentration in terms of ψ becomes

$$\frac{\partial c'}{\partial t} = \frac{1}{\mathrm{ScRa}_s}\left(-\mathrm{Pe}\frac{z}{H}\frac{\partial c'}{\partial z} + \frac{\partial^2 c'}{\partial x^2} + \frac{1}{H^2}\frac{\partial^2 c'}{\partial z^2} + \frac{\partial \psi}{\partial x}\frac{\partial c_0}{\partial z}\right). \tag{18}$$

To find the solution for these coupled equations, a normal-mode form is considered,

$$\psi(x,z,t) = \hat{\psi}(z)e^{(ikx+\sigma t)} + \text{c.c.} \quad \text{and} \quad c'(x,z,t) = \hat{c}(z)e^{(ikx+\sigma t)} + \text{c.c.}, \tag{19}$$

where k gives the modulation of the pattern in the horizontal direction and the sign of the real part of σ indicates the stability of the solution. Using this solution, Eqs. (17) and (18) can be written as a linear system

$$\sigma\begin{pmatrix} D^2-k^2 & 0 \\ 0 & I \end{pmatrix}\begin{pmatrix} \hat{\psi} \\ \hat{c} \end{pmatrix} = \begin{pmatrix} \mathbb{A} & ik \\ \frac{ik}{\text{ScRa}_s}\frac{dc_0}{dz} & \mathbb{B} \end{pmatrix}\begin{pmatrix} \hat{\psi} \\ \hat{c} \end{pmatrix}, \tag{20}$$

with $D = (1/H)d/dz$, and the operators $\mathbb{A}$ and $\mathbb{B}$ are

$$\mathbb{A} = \frac{\text{Pe}}{\text{ScRa}_s}zD(D^2-k^2) + \frac{1}{\text{Ra}_s}(D^2-k^2)^2, \tag{21a}$$

$$\mathbb{B} = \frac{1}{\text{ScRa}_s}[-\text{Pe}zD + (D^2-k^2)]. \tag{21b}$$

In the linear system, dc_0/dz is the numerical derivative of $c_0(z,t)$, which is found by solving Eq. (13). To find the boundary conditions, we recall that the perturbed fluid velocity is $\mathbf{u}(\mathbf{x},t) = \mathbf{0} + \varepsilon\mathbf{u}'(\mathbf{x},t)$ at the leading order. At $z = 0$, $\mathbf{u}' = 0$, this yields

$$u' = \frac{1}{H}\frac{d\psi}{dz} = 0 \quad \text{and} \quad w' = -ik\psi = 0. \tag{22}$$

Since $\psi = \hat{\psi}(z)e^{ikx+\sigma t}$, these conditions imply $\hat{\psi} = d\hat{\psi}/dz = 0$ at $z = 0$. At $z = 1$, there is a free surface and no vertical velocity, $w' = 0$, which implies $\hat{\psi} = 0$. Similarly, imposing the zero-stress condition (see also [30]) gives

$$\frac{1}{H}\frac{\partial u'}{\partial z} + \frac{\partial w'}{\partial x} = 0, \tag{23}$$

which in terms of the stream function ψ is equivalent to $(1/H^2)d^2\psi/dz^2 = 0$. Thus, at $z = 1$, $\hat{\psi} = d^2\hat{\psi}/dz^2 = 0$. The boundary conditions for $\hat{c}$ are given by $d\hat{c}/dz = 0$ at $z = 0$ and $d\hat{c}/dz = \text{Pe}H\hat{c}$ at $z = 1$ from (4b) and (4c).

D. Numerical implementation

A numerical solution to the governing equations begins with the solution of Eq. (13), which yields the salt concentration profile $c_0(z)$ at a given time $t_0(=T/\delta)$. Then, Eq. (20) is solved by discretizing the interval $z = [0, 1]$ into $N = 100$ equally spaced nodes, and the derivatives are calculated using second-order central finite differences. Since the matrices have size $2N \times 2N$, there are $2N$ eigenvalues and $2N$ eigenvectors, but because the equations for the boundary conditions were explicitly written into the matrices, there are six spurious eigenvalues, which can be easily discarded from the final solution. We identify the eigenvalue with the largest real part, as this corresponds to the fastest growing mode. The corresponding eigenvector contains the information about $\hat{\psi}$ and $\hat{c}$ for the mode which leads to the instability. In order to test the code, the traditional Rayleigh-Bénard convection was solved for rigid-rigid boundary conditions, obtaining a neutral stability curve that compares very well to the standard result [30]. The physical parameters used to solve the linear system are shown in Table II. The value of β was taken from Kang *et al.* [20], and the evaporation speed was measured experimentally.

E. Results

Considering the salt profile at $t_0 = 1$ h, the largest eigenvalues were calculated for different wavevectors k and salinity Rayleigh numbers. Figure 10 shows the k-Ra_s plane color coded by the

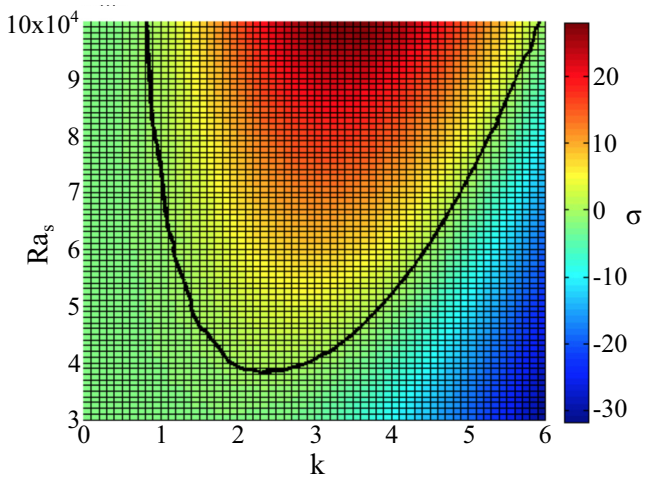

FIG. 10. Stability analysis. Values of the largest eigenvalue σ in the plane of salinity Rayleigh number Ra_s and wave vector k. In black is the neutral stability curve. Parameters are those in Table II.

value of the growth rate σ, and the neutral stability curve along which $\sigma = 0$. The smallest critical Rayleigh number is $\mathrm{Ra}_s^* = 3.8 \times 10^4$, with a critical wave number $k^* = 2.3$. From the definition of the salinity Rayleigh number, this occurs at a salt concentration of $5 \times 10^{-4}\%$ (w/w), and implies a critical wavelength of 2.73 cm. A comparison with experiments is given in Sec. V.

Varying Schmidt and Péclet numbers. The results above were obtained for $\mathrm{Pe} = 0.2$ and $\mathrm{Sc} = 1000$. The neutral stability curve for $\mathrm{Sc} = 1$ is essentially identical to the one for $\mathrm{Sc} = 1000$, but the eigenvalues are different. This result is also obtained in the Rayleigh-Bénard instability, in which case it is possible to demonstrate analytically that the Schmidt number does not affect the condition for stability but it does affect the magnitude of the eigenvalues [30]. Conversely, and as shown in Fig. 11, a higher Péclet number has the effect of lowering the critical Rayleigh number as well, making the neutral stability curve broader. These results are expected from the definition of the Péclet number $\mathrm{Pe} = h_0 v_e / D$. A higher value can be achieved for example by increasing the evaporation rate, which increases the salt accumulation at the top. From the plots in Fig. 11 one can see that a higher Péclet number also has the effect of increasing the value of the largest eigenvalue, which results in the instability appearing sooner.

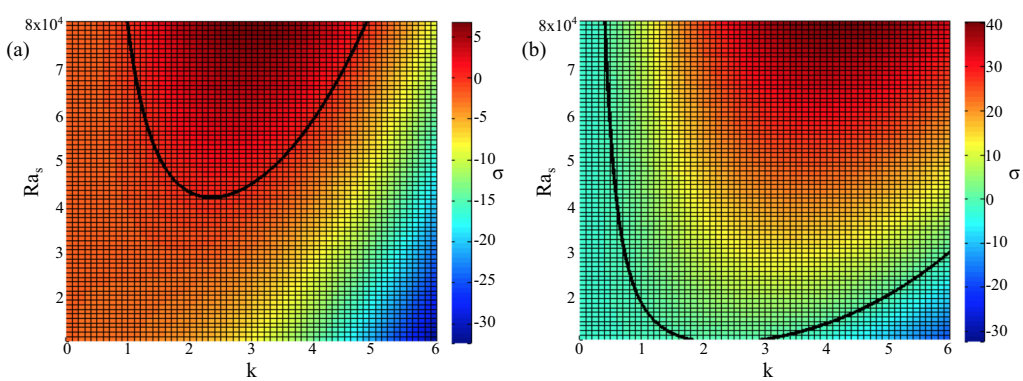

FIG. 11. Effect of Péclet number on the neutral stability curve. (a) $\mathrm{Pe} = 0.1$ and $\mathrm{Sc} = 1$, (b) $\mathrm{Pe} = 0.4$ and $\mathrm{Sc} = 1$.

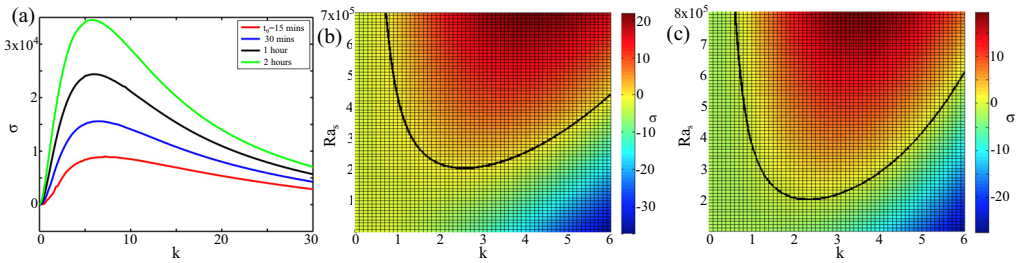

FIG. 12. Effects of varying t_0. (a) Largest eigenvalue for different choices of t_0, with Pe $= 0.2$ and $\mathrm{Ra}_s = 6.6 \times 10^7$. Neutral stability curves for $t_0 = 15$ min (b) and $t_0 = 2$ hours (c), both with Sc $= 1$ and Pe $= 0.2$.

Varying the time at which the base state is calculated: t_0. All the results shown above were obtained by considering that the base state is reached within 1 hour, independent of the initial salt concentration; the salt profile has been calculated according to Eq. (13) and evaluated at time t_0 (=1 hour). As the dimensionless height was assumed to be constant in the linearized equations $H(t_0) = H_0$, the choice of t_0 also affects the value of H_0. Nevertheless, the evaporation speed is so small that the height decreases only 1 mm in 10 hours.

Figure 12(a) shows the largest eigenvalue σ as a function of k when the base state is calculated after 15, 30, 60, and 120 minutes. As expected, the longer one waits, the more salt has accumulated at the top, and the faster the convection starts. Nevertheless, the position of the peak remains almost the same; the wavelength of the pattern is not significantly dependent of the choice of t_0. Figure 12 shows the neutral stability curve for (b) $t_0 = 15$ minutes and (c) at $t_0 = 2$ hours. Comparing these figures to Fig. 10 (for $t_0 = 1$ hour) one observes that the choice of t_0 modifies the value of the critical salinity Rayleigh number without changing the critical wavelength significantly.

The diffusive development of an unstable concentration gradient in the base state occurs on the time scale

$$T_{\mathrm{base}} \sim O\left(h_0^2/D\right) \sim O(10^3) \text{ minutes.} \tag{24}$$

for $h_0 = 0.01$ m and $D = 1 \times 10^{-9}$ m^2/s. We would therefore expect that the critical Rayleigh number for the instability should have a strong dependence on the waiting time t_0 when $t_0 < T_{\mathrm{base}}$, and this is confirmed in Fig. 13, where we see that for a given Pe the critical Ra_s decreases very rapidly for $t_0 \leqslant 50$ min. This suggests that the evaporation-driven convection would occur within this time scale if the salt concentration is sufficiently high. For example, with a salt concentration of 0.1% (equivalent to $\mathrm{Ra}_s = 0.68 \times 10^5$), the convection instability would start at $t_0 \simeq 25$ min, providing a consistent comparison with the experiment [see Fig. 7(a)] and numerical simulations. However, it should be noted that the critical Rayleigh number curve with respect to t_0 in Fig. 13 would not be precisely valid when the growth rate of the linear instability is extremely small, for it could then be comparable to the evaporation rate, violating the quasi-steady assumption made in the linear stability analysis.

IV. TWO-DIMENSIONAL FINITE ELEMENT STUDIES

Since the linear stability analysis would not be valid in the regime far beyond the critical Rayleigh number, where nonlinearities would become important, we investigated this regime numerically. For simplicity, a two-dimensional geometry was used, shown in Fig. 14. As in the experiments, the initial height of the column of water is $h_0 = 1$ cm, the length of the cuvette is 6 cm, and the salt concentration is initially homogeneous and equal to c_0. For the numerical computations, Eqs. (4a), (3a), and (3b) are rescaled using the following expressions for length, time, flow speed, pressure,

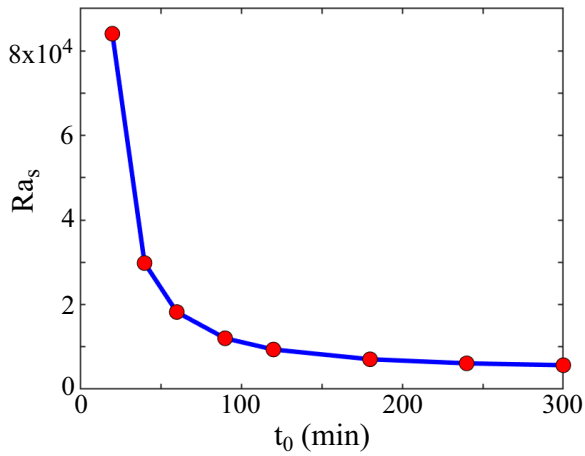

FIG. 13. Effects of varying t_0. Critical salinity number for a range of base-state waiting times t_0, with $\mathrm{Pe} = 0.2$.

and salt concentration:

$$\mathbf{x} = \frac{\mathbf{x}^*}{h_0}, \quad t = \frac{D}{h_0^2} t^*, \quad \mathbf{u} = \frac{h_0}{D}\mathbf{u}^*, \quad p = \frac{h_0^2}{\rho_0 D^2} p^*, \quad c = \frac{c^*}{c_0}.$$

The dimensionless equations to be solved numerically are then

$$\nabla \cdot \mathbf{u} = 0, \tag{25a}$$

$$\frac{\partial \mathbf{u}}{\partial t} + \mathbf{u} \cdot \nabla \mathbf{u} = -\nabla p + \mathrm{Sc}\nabla^2 \mathbf{u} - \mathrm{RaSc}(c-1)\hat{\mathbf{z}}, \tag{25b}$$

$$\frac{\partial c}{\partial t} + \mathbf{u} \cdot \nabla c = \nabla^2 c. \tag{25c}$$

The numerical studies were performed using the finite element package COMSOL MULTIPHYSICS, in which, as in previous sections, the Navier-Stokes equation for the fluid was coupled to the advection-diffusion equation for the salinity. The program was benchmarked on the traditional Rayleigh-Bénard convection with solid-solid boundaries, obtaining a critical Rayleigh number of $\simeq$1700, in good agreement with the known result of 1707.7 [30]. Here, the boundary conditions for the fluid were nonslip at the lateral and bottom sides, and force-free at the top boundary. The buoyancy force due to the salt concentration was implemented using the "Volume Force" feature of COMSOL. At the lateral and bottom sides, the boundary conditions for the salt concentration were no-flux. COMSOL can handle the moving top boundary due to evaporation by use of the "Deformable Geometry" module, which works as follows: the equations for the fluid flow and salt concentration are written considering a fixed height h_0, and an equation for the movement of the top boundary is specified. The code then calculates a new mesh by propagating the deformation throughout the

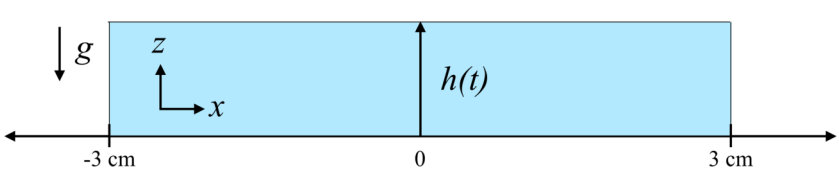

FIG. 14. Geometry for full numerical studies.

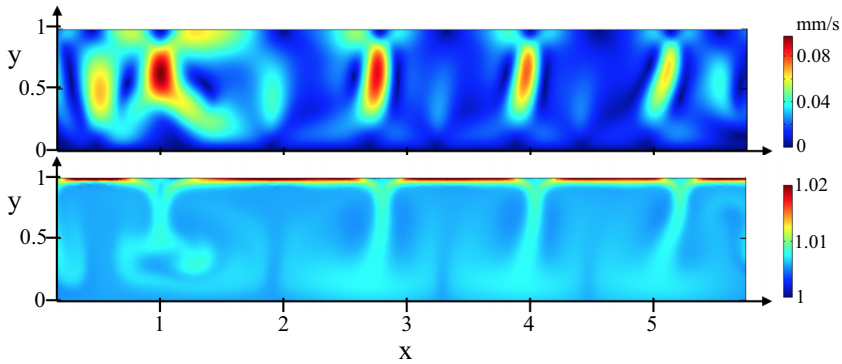

FIG. 15. Numerical results for 1% (w/w) initial salt concentration and 60 minutes after the experiment has started. Top: flow field; bottom: normalized salt concentration.

domain. Material is added or removed depending on the movement of the boundaries, so the total concentration of species is not conserved between iterations [31]. Because in the present problem the total amount of salt must be conserved, a flux of salt is added at the top, given by $v_e c$, where v_e is the dimensionless rate of evaporation (measured experimentally) and c is the dimensionless salt concentration at the top surface. The mesh used was the predefined normal mesh calibrated for fluid dynamics, with a maximum element size 0.045 and minimum element size 0.002. In addition, a corner refinement was added in such way that the elements at the boundaries are scaled by a factor 0.25. The numerical values for the parameters in the simulations are the ones shown in Table II.

The COMSOL simulation was also verified by imposing periodic boundary conditions (pbc) in the horizontal direction. In this case, the given horizontal domain size only allows the simulation to resolve 6 cm/n of horizontal wavelengths ($n = 1, 2, 3, \ldots$). For 1% of salt concentration, the distance between initially developing plumes was found to be $\lambda_{pbc,1\%} = 1$ cm, showing excellent agreement with $\lambda_{\text{linear},1\%} = 1.05$ cm obtained from the linear stability analysis. In the following discussion, we will focus on comparison of the experimental data with COMSOL simulation result obtained with no-slip condition for fluid and no-flux condition for salt concentration.

Figure 15 shows the numerical results for experiments with 1% (w/w) salt concentration. The flow speed (in mm/s) and the salt concentration (normalized by its initial value) are shown 60 minutes after the experiment had started. Here one can see the correspondence between high concentrations of salt and the position of the plumes. These numerics also show the rich plume dynamics noticed in the experiments (see Videos 4 and 5 of the Supplemental Material [27]). In both cases the number of plumes is not constant and coalescence events are observed.

The average distance between plumes can be calculated from these images using a code similar to the one described in Sec. II, using the color coding of the velocity field to identify plumes. After the image was cropped to narrow it in the vertical direction, it was converted to black and white with a threshold of 0.2, and the pixels were averaged vertically. This analysis gives a separation between plumes, averaged over time, of $\lambda_{\text{sim},1\%} = 0.83 \pm 0.17$ cm, which is in good agreement with $\lambda_{\text{exp},1\%} = 0.67 \pm 0.06$ cm measured experimentally, and the linear stability result $\lambda_{\text{linear},1\%} = 1.05$ cm (further comparisons between the three approaches are given in the next section). It is important to note that in the numerical simulations the variation in plume separation with salt concentration is smaller than in the experiments.

In the experiments it was clear that the lower the overall salt concentration, the longer it takes for plumes to develop, which can be understood from the fact that a longer time is needed to accumulate sufficient salt at the top boundary. As can be seen in Fig. 16, this feature is also observed in the simulations. Here, the snapshots were taken when the plumes first developed, which is longer as the initial salt concentration decreases. In addition, the flow field magnitude also decreases with

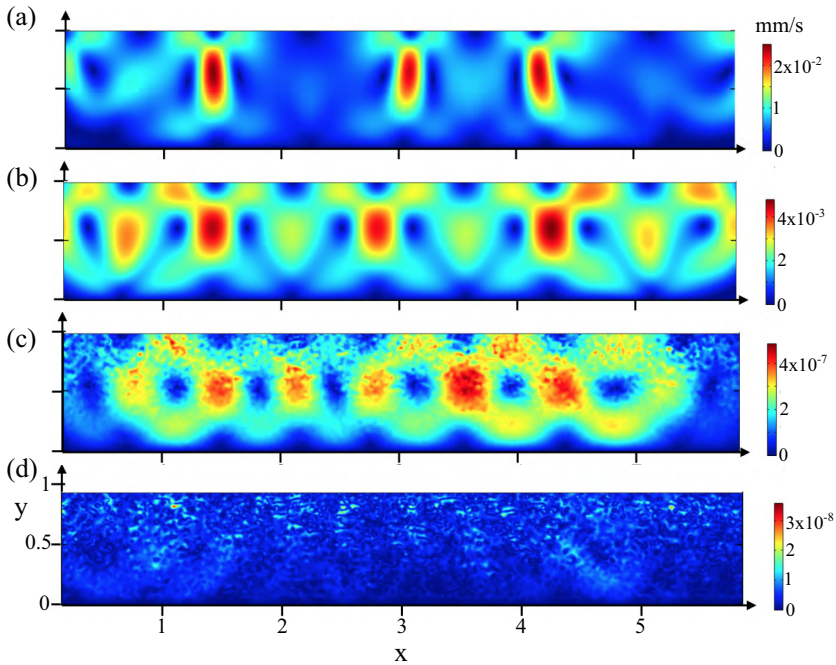

FIG. 16. Numerical flow fields for different initial salt concentrations. Snapshots at times corresponding to appearance of plumes for (a) 0.1% at $t = 45$ min., (b) 0.01% at $t = 120$ min, (c) 0.001% at $t = 180$ min, and (d) 0.0001% at 10 hours, at which point no plumes were observed.

lower initial salt concentrations, which is expected since there is less salt being accumulated at the air-water interface.

V. COMPARISON BETWEEN EXPERIMENTS, LINEAR STABILITY ANALYSIS, AND NUMERICAL SIMULATIONS

Here we summarize some of the quantitative measurements of plume obtained using the three approaches. We recall that in the linear stability analysis an infinite two-dimensional system was considered, while in the experiments and numerical simulations the system was laterally finite, so geometric confinement effects can occur. Moreover, in the experiments, the cuvette of course had front and back glass walls, so that the dynamics might be considered more akin to Hele-Shaw flow than a truly two-dimensional system.

Separation between plumes. For 1% salt concentration experiments, the time average over many well-developed plumes gave a separation of $\lambda_{\mathrm{exp},1\%} = 0.67 \pm 0.06$ cm. From the linear stability analysis, which of course only applies to the very onset of the instability, the expected separation is $\lambda_{\mathrm{linear},1\%} = 1.05$ cm, while for the same salt concentration the full nonlinear numerical simulations gave $\lambda_{\mathrm{sim},1\%} = 0.83 \pm 0.17$ cm. When the initial salt concentration was 0.1% (w/w), the average separation between plumes was $\lambda_{\mathrm{exp},0.1\%} = 1.58 \pm 0.08$ cm, that compares well to the value given by the linear stability analysis of $\lambda_{\mathrm{linear},0.1\%} = 1.43$ cm.

Minimal salt concentration needed to observe plumes. Linear stability analysis predicted that the critical salt concentration to observe plumes is $5 \times 10^{-4}\%$ (w/w), which is in good agreement with the numerical simulations, in which we did not observe plumes for $10^{-4}\%$ salt, but slow plumes could be identified for $10^{-3}\%$. On the other hand, in experiments the lowest salt concentration for which we could identify plumes was $10^{-2}\%$ (w/w). This discrepancy can be due to multiple factors,

including, as mentioned above, the presence of lateral walls and the added viscous drag associated with the experimental Hele-Shaw geometry.

Time required to observe plumes. Experimental observations indicate that when using 1% (w/w) salt concentration the instability developed within 15 minutes, while for 0.1% (w/w) plumes appeared 2 hours after the experiment had started (i.e., 8 times longer for a 10 times more dilute suspension). Likewise, in the linear stability analysis, the time needed for the instability to start is reflected in the value of the largest eigenvalue, which was 7 times larger for 1% salt concentration than for 0.1%, in fairly good agreement with experiment. On the other hand, the analysis in the case of full numerical simulations gives a ratio of only $\sim$3 between the time needed to identify plumes in suspensions with 0.1% salt compared to those 1%. The most probable reason of this discrepancy would be due to the presence of two walls (i.e., two coverslips in Fig. 2) parallel to the x-z plane in the experiment, which are not implemented in the two-dimensional COMSOL simulation. These walls are likely to generate friction in the initial plume development and delay the time needed to see well-developed plumes.

VI. CONCLUSIONS

We have proposed that accumulation of salt due to evaporation can explain the convective patterns observed in suspensions of a nonmotile marine bacterium. This hypothesis was studied using control experiments with microspheres of various sizes suspended in growth media with varying salinity. A mathematical model similar in spirit to that used for bioconvection was developed—but focusing on the salt flux created by evaporation at the suspension's upper surface—and was studied by linear stability analysis and fully nonlinear numerical simulations. The key dimensionless quantity in the model is the salinity Rayleigh number, the critical value of which corresponds to the the threshold of salt concentration needed to observe plumes, and which determines the wavelength at the onset of the instability. Both results compare well with experimental observations. Similarly, finite-element method simulations showed a plume dynamics very similar to those in experiment, and the dependence on the salt concentration is in agreement with the results obtained using the other two methods.

The phenomenon of interest here was discovered in a suspension of nonmotile marine bacteria, but plumes were also observed using a nonmarine bacterium (*Serratia*) with low salt concentration in the medium. Therefore the convection does not require salt in particular, but merely *some* component that accumulates due to evaporation. The accumulation of solute is always present in experiments with an open-to-air surface, and this effect may have been underestimated in other systems. For the bacterial medium used, the patterns appeared within 15 minutes, which may certainly be comparable to the duration of typical laboratory experiments. On the other hand, when using motile bacteria, the directed movement (chemotaxis) of cells toward the suspension-air interface is likely to be much stronger than the convection created by solute accumulation [32].

In the ocean, an accumulation of salt can generate "salt fingers," which are formed when cold fresh water surrounds warm salty water. This phenomenon relies on the fact that thermal diffusion is faster than the salt diffusion, which has the consequence that a region high in salt will cool before the salt can diffuse, creating a descending plume of dense salty water [33]. In the ocean this instability has a profound effect on mixing, which influences factors such as the availability of nutrients, heat storage, dispersal of pollutants, and the fixation of carbon dioxide, among others [34]. An analogy between the convection in the ocean and the fluid flow observed in a suspension of nonmotile *P. phosphoreum* is particularly interesting, as one could argue that the motion created by evaporation may enhance nutrient mixing. The possibility that bioconvective enhancement of mixing may improve population-level growth has been considered previously and found not to occur [35]. The relevance of a mixing effect on microorganisms associated with evaporation remains to be studied quantitatively, as does its effect on the so-called "sea surface microlayer," the submillimeter interfacial layer within which much important geobiochemistry occurs [36].

ACKNOWLEDGMENTS

We are grateful to François Peaudecerf for assistance in constructing the bacterial growth curve, Rita Monson for assistance with *Serratia* and Andrew Berridge for comments on the manuscript. This research was supported in part by ERC Advanced Investigator Grant No. 247333, EPSRC Established Career Fellowship EP/M017982/1, and Grant 7523 from the Gordon and Betty Moore Foundation (R.E.G.). J.D. received support via a Ph.D. fellowship from the Chilean government (Becas Chile) and is supported by CMM-Basal AFB 170001. K.J.L. was supported by the Basic Science Research Program through the National Research Foundation of Korea (NRF) funded by the Ministry of Education (Grant No. 2016R1D1A1B03930591).

APPENDIX

The boundary condition for c at the free surface is sought here. Using the Leibniz integral rule, let us write the temporal change of the salt concentration over the entire control volume as follows:

$$\int_{-\infty}^{\infty}\int_{0}^{\zeta(t^*,x^*)}\frac{\partial c^*}{\partial t^*}dz^*dx^* = \frac{\partial}{\partial t^*}\left(\int_{V(t^*,x^*)} c^* dV^*\right) - \int_{-\infty}^{\infty} c^*(x^*,\zeta(t^*,x^*),t^*)\frac{\partial \zeta}{\partial t^*}dx^*, \quad \text{(A1)}$$

where $\zeta(t^*,x^*) = h(t^*) + \eta(t^*,x^*)$ and $V = [-\infty,\infty]\times[0,\zeta(t^*,x^*)]$. The first term on the right-hand side of (A1) is the change rate of the total amount of salt in the system, and the second term represents the rate of change of the salt concentration due to evaporation over the entire free surface. We note that the first term should vanish because the total amount of salt in the system is constant. This implies that the integrand of the second term represents the rate of change of the salt concentration at a given location x^* on the free surface. Then, the conservation of the total salt concentration requires the following boundary condition at the free surface:

$$(-\mathbf{u}^* c^* + D\nabla c^*)\cdot\hat{\mathbf{k}} = \left(v_e - \frac{\partial \eta}{\partial t^*}\right)c^* \quad \text{at} \quad z^* = \zeta, \quad \text{(A2)}$$

where the constant evaporation rate v_e was identified.

[1] J. J. Farmer III and F. W. Hickman-Brenner, The genera *Vibrio* and *Photobacterium*, Prokaryotes **6**, 508 (2006).
[2] P. Dunlap and K. Kita-tsukamoto, Luminous bacteria, Prokaryotes **2**, 863 (2006).
[3] J. J. Bourgois, F. E. Sluse, F. Baguet, and J. Mallefet, Kinetics of light emission and oxygen consumption by bioluminescent bacteria, J. Bioenerg. Biomembr. **33**, 353 (2001).
[4] T. J. Pedley and J. O. Kessler, Hydrodynamic phenomena in suspensions of swimming microorganisms, Annu. Rev. Fluid Mech. **24**, 313 (1992).
[5] A. J. Pons, F. Sagués, M. A. Bees, and P. G. Sorensen, Pattern formation in the methylene-blue–glucose system, J. Phys. Chem. B **104**, 2251 (2000).
[6] M. R. Benoit, R. B. Brown, P. Todd, E. S. Nelson, and D. M. Klaus, Buoyant plumes from solute gradients generated by non-motile *Escherichia coli*, Phys. Biol. **5**, 046007 (2008).
[7] W. G. Spangenberg and W. R. Rowland, Convective circulation in water induced by evaporative cooling, Phys. Fluids **4**, 743 (1961).
[8] J. C. Berg, M. Boudart, and A. Acrivos, Natural convection in pools of evaporating liquids, J. Fluid Mech. **24**, 721 (1966).
[9] J. R. Saylor, G. B. Smith, and K. A. Flack, An experimental investigation of the surface temperature field during evaporative convection, Phys. Fluids **13**, 428 (2001).
[10] H. Mancini and D. Maza, Pattern formation without heating in an evaporative convection experiment, Europhys. Lett. **66**, 812 (2004).

[11] H. Machrafi, A. Rednikov, P. Colinet, and P. C. Dauby, Benard instabilities in a binary-liquid layer evaporating into an inert gas, J. Colloid Interface Sci. **349**, 331 (2010).
[12] J. T. Kimball, J. C. Hermanson, and J. S. Allen, Experimental investigation of convective structure evolution and heat transfer in quasi-steady evaporating liquid films, Phys. Fluids **24**, 052102 (2012).
[13] K. Matthiessen, H. Wilke, and S. C. Müller, Influence of surface tension changes on hydrodynamic flow induced by traveling chemical waves, Phys. Rev. E **53**, 6056 (1996).
[14] W. Paxton, A. Sen, and T. E. Mallouk, Motility of catalytic nanoparticles through self-generated forces, Chem. Eur. J. **11**, 6462 (2005).
[15] F. Chauvet, S. Dehaeck, and P. Colinet, Threshold of Bénard-Marangoni instability in drying liquid films, Europhys. Lett. **99**, 34001 (2012).
[16] F. Doumenc, T. Boeck, B. Guerrier, and M. Rossi, Transient Rayleigh-Bénard-Marangoni convection due to evaporation: A linear non-normal stability analysis, J. Fluid Mech. **648**, 521 (2010).
[17] G. Toussaint, H. Bodiguel, F. Doumenc, B. Guerrier, and C. Allain, Experimental characterization of buoyancy- and surface tension-driven convection during the drying of a polymer solution, Int. J. Heat Mass Transfer **51**, 4228 (2008).
[18] J. Zhang, A. Oron, and R. P. Behringer, Novel pattern forming states for Marangoni convection in volatile binary liquids, Phys. Fluids **23**, 072102 (2011).
[19] H. Masoud and M. J. Shelley, Collective Surfing of Chemically Active Particles, Phys. Rev. Lett. **112**, 128304 (2014).
[20] K. H. Kang, H. C. Lim, H. W. Lee, and S. J. Lee, Evaporation-induced saline Rayleigh convection inside a colloidal droplet, Phys. Fluids **25**, 042001 (2013).
[21] R. Brown, Additional remarks on active molecules, Philos. Mag. Ser. **6**, 161 (1829).
[22] R. D. Deegan, O. Bakajin, T. F. Dupont, G. Huber, S. R. Nagel, and T. A. Witten, Capillary flow as the cause of ring stains from dried liquid drops, Nature (London) **389**, 827 (1997).
[23] L. Rayleigh, LIX. On convection currents in a horizontal layer of fluid, when the higher temperature is on the under side, London Edinburgh Dublin Philos. Mag. J. Science **32**, 529 (1916).
[24] O. P. Singh and J. Srinivasan, Effect of Rayleigh numbers on the evolution of double-diffusive salt fingers, Phys. Fluids **26**, 062104 (2014).
[25] R. A. Wooding, S. W. Tyler, and I. White, Convection in groundwater below an evaporating salt lake. 2. Evolution of fingers or plumes, Water Res. Research **33**, 1219 (1997).
[26] B. Stevenson, *Common Bacterial Culture Techniques and Media - Current Protocols in Microbiology* (John Wiley and Sons, New York, 2006).
[27] See Supplemental Material at http://link.aps.org/supplemental/10.1103/PhysRevFluids.3.123102 for videos of experimental results and numerical studies.
[28] H. Bénard, Les tourbillons cellulaires dans une nappe liquide. Méthodes optiques d'observation et d'enregistrement, J. Phys. Theor. Appl. **10**, 254 (1901).
[29] Y. Renardy and R. Schmitt, Linear stability analysis of salt fingers with surface evaporation or warming, Phys. Fluids **8**, 2855 (1996).
[30] P. G. Drazin and W. H. Reid, *Hydrodynamic Stability*, 2nd ed. (Cambridge University Press, Cambridge, 2004).
[31] Comsol Multiphysics Reference Manual, version 5.0, 2014.
[32] I. Tuval, L. Cisneros, C. Dombrowski, C. W. Wolgemuth, J. O. Kessler, and R. E. Goldstein, Bacterial swimming and oxygen transport near contact lines, Proc. Natl. Acad. Sci. USA. **102**, 2277 (2005).
[33] R. Schmitt, Double Diffusion in Oceanography, Annu. Rev. Fluid Mech. **26**, 255 (1994).
[34] H. E. Huppert and J. S. Turner, Double-diffusive convection, J. Fluid Mech. **106**, 299 (1981).
[35] I. M. Jánosi, A. Czirók, D. Silhavy, and A. Holczinger, Is bioconvection enhancing bacterial growth in quiescent environments? Env. Microbiol. **4**, 525 (2002).
[36] M. Cunliffe, A. Engel, S. Frka, B. Gasparović, C. Guitart, J. C. Murrell, M. Salter, C. Stolle, R. Upstill-Goddard, and O. Wurl, Sea surface microlayers: A unified physicochemical and biological perspective of the air-ocean interface, Prog. Ocean. **109**, 104 (2013).